



Urban impacts on a cold-frontal precipitation system passing over the Seoul metropolitan area: An ensemble simulation study

Seong-Ho Hong, Jong-Jin Baik*

School of Earth and Environmental Sciences, Seoul National University, Seoul 08826, South Korea

ARTICLE INFO

Keywords:

Urban impacts
Cold-frontal precipitation
Cross-frontal vorticity
Frontal updraft
Urban heat island
Ensemble simulations

ABSTRACT

Precipitation systems passing over cities can be modified by urban impacts. Compared with urban impacts on less-organized convective precipitation systems, urban modification of highly-organized or strongly-forced precipitation systems remains less understood. In this study, we examine urban impacts on a cold-frontal precipitation system passing over the Seoul metropolitan area, South Korea. For this, three sets of urban ensemble simulations with diurnal-mean anthropogenic heat intensities and urban momentum roughness lengths of (0 W m^{-2} , 1 m), (45 W m^{-2} , 2 m), and (90 W m^{-2} , 3 m) and a set of nonurban ensemble simulations are performed. Comparisons with observations show that the characteristics and passage of the cold front are acceptably reproduced in all sets of the ensemble simulations. Precipitation is enhanced by about 20–40 % downstorm of Seoul in the urban ensemble simulations, with marginal delays in the movement of the precipitation system. The precipitation enhancement is hard to be discerned by a comparison between a single pair of urban and nonurban simulations, since the urban-induced precipitation enhancement is obscured by strong precipitation anomalies arising from different locations of precipitation cores in individual simulations. The downstorm precipitation enhancement is attributed to precipitation intensity increases in narrow cold-frontal rainband, which results from intensified frontal updrafts due to the increases in cross-frontal vorticity. The warm urban-heated air trailing the cold front after the frontal passage results in the increases in cross-frontal vorticity by decreasing temperature gradient at the frontal zone.

1. Introduction

Precipitation in and around cities has great influences on urban residents. The precipitation can disrupt traffic and transport (e.g., Andrey et al., 2003; Chung, 2012), impact water resources (e.g., Dabrowska et al., 2023), and often cause significant economic losses and casualties (WMO, 2021; MOIS, 2024; NCEI, 2025). This makes in-depth understanding and accurate prediction of urban precipitation vital. One of the influential factors in precipitation in and around cities is the impacts of urban areas on the lower atmosphere such as the urban heat island (UHI), the deceleration and/or diversion of flows due to urban drag from large urban surface roughness, and the emission of anthropogenic aerosols. These can cause thermal, dynamical, and microphysical changes in precipitation systems (Han et al., 2014; Oke et al., 2017; Yue et al., 2021; Qian et al., 2022), altering precipitation distribution in and around cities (Changnon et al., 1977; Liu and Niyogi, 2019; IPCC, 2023).

Urban impacts on less-organized convective precipitation systems

have been well studied through previous numerical modeling studies, with important roles of the UHI having been reported. The UHI can initiate moist convection by inducing convergent flows and accompanying updrafts (Baik et al., 2001; Han and Baik, 2008) and/or by elevating boundary-layer top height (Li et al., 2017; Sun et al., 2021). In coastal cities, the UHI can help development of the precipitation systems by strengthening sea-breeze penetration and resultant moisture transport toward urban areas (Fan et al., 2020; Doan et al., 2021; Sun et al., 2021). The UHI impacts were relatively frequently reported in afternoon/evening and/or in warm seasons (e.g., Seino et al., 2018; Simón-Moral et al., 2021) whose conditions are favorable for convection development. Meanwhile, the urban drag impacts were reported to be less pronounced than the UHI impacts (Thielen et al., 2000; Rozoff et al., 2003; Kusaka et al., 2019).

Highly-organized or strongly-forced precipitation systems account for a large portion of regional precipitation (e.g., Utsumi et al., 2014; Haberlie and Ashley, 2019; Rüdisühli et al., 2020) and/or are often associated with severe weather-related disasters (e.g., Rappaport, 2014;

* Corresponding author.

E-mail address: jjbaik@snu.ac.kr (J.-J. Baik).

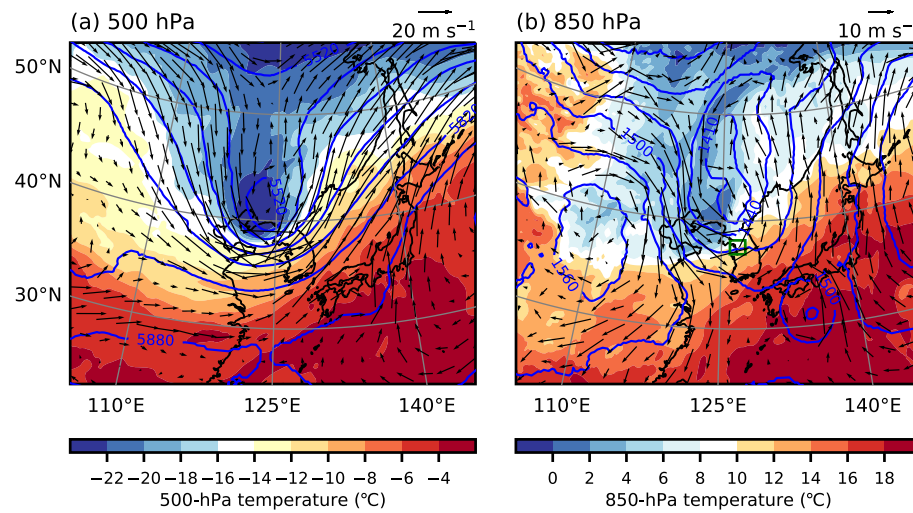


Fig. 1. Fields of temperature (shades), geopotential height (blue contours), and wind vector (arrows) at (a) 500- and (b) 850-hPa levels at 1100 LST on 23 September 2022. The contours for geopotential height are plotted with 60 m intervals for the 500-hPa level and 30 m intervals for the 850-hPa levels. The green box in (b) indicates the location of the SMA. (For interpretation of the references to colour in this figure legend, the reader is referred to the web version of this article.)

Ralph et al., 2019; Hu et al., 2021). Urban impacts on these systems have been relatively less examined compared with those on the less-organized systems but recently receive increasing attention. Through numerical simulations, Zhang et al. (2018) examined urban impacts on a land-falling tropical cyclone, hurricane Harvey, in Houston, USA. They suggested that the urban drag impacts enhance low-level convergence and updrafts, increasing total precipitation of Harvey. Reames and Stensrud (2018) examined urban impacts on a supercell storm in Oklahoma, USA using simulations in which the location of urban areas relative to supercell is varied. They reported that urban impacts can lead to statistically significant differences in mesocyclone strength, changing with the location of urban areas. Yang et al. (2019) examined urban impacts on an extreme monsoon rainfall event in Phoenix, USA using simulations. They showed that when large precipitation is produced by orographic lifting of monsoon flow, the urban drag impacts intensify precipitation near urban–rural boundary by decelerating downslope cold outflows and assisting secondary uplift there. These results imply that how urban impacts modify highly-organized or strongly-forced precipitation systems may vary with the dynamical structure of the systems, necessitating examinations with considerations of their distinct dynamical characteristics.

Cold-frontal precipitation system is a highly-organized and strongly-forced precipitation system, being one of the major precipitation parts of extratropical cyclone (Houze, 2014). Cold-frontal precipitation system features narrow intense rainband with strong and shallow (likely, < 3 km) forced updraft at the front (e.g., Clark, 2023; Zou et al., 2023), often accompanied by stratiform precipitation. The narrow intense rainband may be composed of precipitation cores and gaps where precipitation intensity is relatively strong and weak, respectively (e.g., Jorgensen et al., 2003; Norris et al., 2017). Ahead of the cold front, low-level jet parallel to the front is present, playing an important role in moisture transport from the south (e.g., Ralph et al., 2004; Gimeno et al., 2014). Behind the cold front, strong wind in the lower troposphere brings about cold advection, which is associated with the advance of the front (e.g., Markowski and Richardson, 2010; Mak et al., 2017).

Several studies investigated urban impacts on cold front and/or cold-frontal precipitation system (Loose and Bornstein, 1977; Gaffen and Bornstein, 1988; Zhong and Yang, 2015a, 2015b). Earlier observational studies found retarded passage of cold front over New York City, USA and suggested the urban drag impacts as a possible cause (Loose and Bornstein, 1977; Gaffen and Bornstein, 1988). Using ensemble simulations of a cold-frontal precipitation event in the Great Beijing metropolitan area (GBMA), China, Zhong and Yang (2015a) showed that

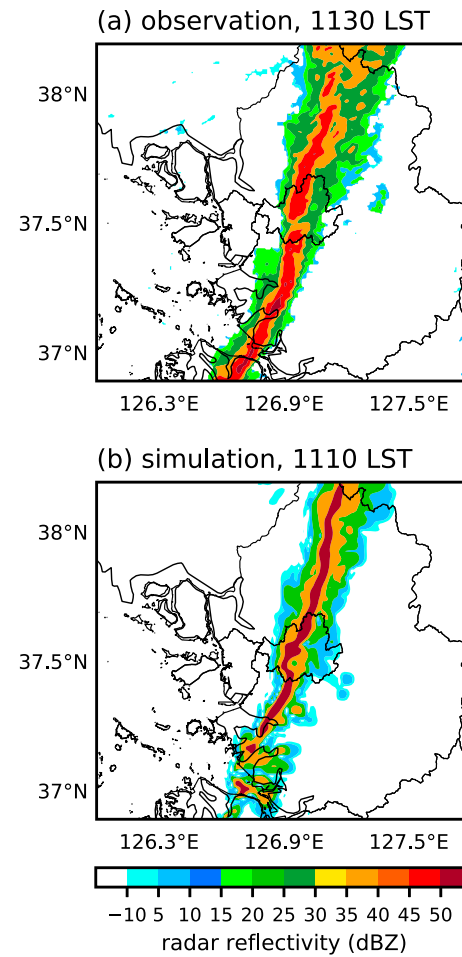


Fig. 2. Fields of radar reflectivity (constant altitude plan position indicator at $z = 1.5$ km MSL) (a) at 1130 LST for the multi-radar composite and (b) at 1110 LST for a single ensemble member of the URBAN1 ensemble simulations on 23 September 2022.

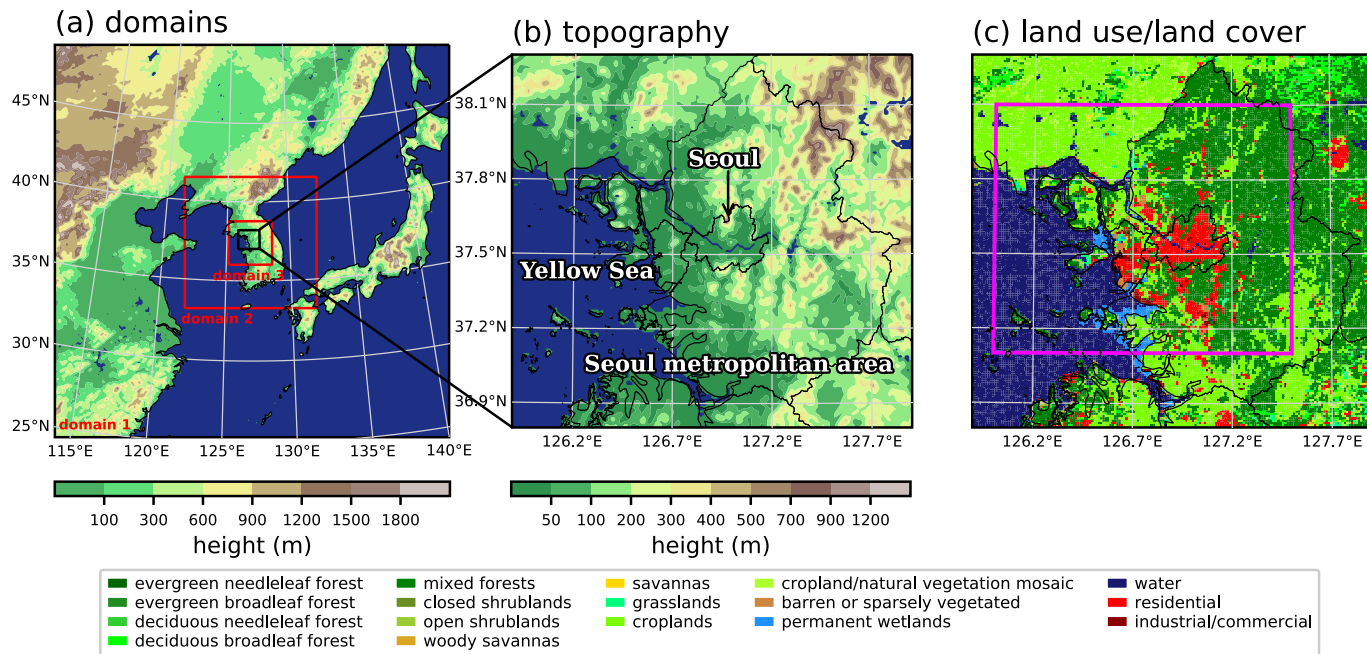


Fig. 3. (a) Configuration of three one-way nested domains and (b) topography in and around the SMA. (c) Land use/land cover map in and around the SMA. The pink box in (c) indicates where anthropogenic heat intensity and urban momentum roughness length are changed in the urban ensemble simulations and urban grids are replaced with cropland grids in the NO-URBAN ensemble simulations. (For interpretation of the references to colour in this figure legend, the reader is referred to the web version of this article.)

urban impacts can cause changes in timing and spatial distribution of cold-frontal precipitation in and around the GBMA. In their following work (Zhong and Yang, 2015b), they showed that urban impacts delay the passage of cold front by weakening cold advection, which leads to the delayed onset of frontal precipitation in the urban area of the GBMA. While the urban impacts on passage of cold front were examined by the studies, how urban modification of cold front affects frontal updraft and resultant cold-frontal precipitation has been little investigated.

In this study, we examine urban impacts on a cold-frontal precipitation system passing over the Seoul metropolitan area (SMA), South Korea using ensemble simulations. The dynamical processes involved in the urban impacts on frontal updraft and cold-frontal precipitation are investigated in detail. In Section 2, the precipitation event of interest is described and experimental design is explained. In Section 3, results and discussion are presented. In Section 4, summary and conclusions are given.

2. Method

2.1. Case description

On 23 September 2022, a cold-frontal precipitation system passed over the SMA, accumulating precipitation in the late morning and early afternoon. Fig. 1a and b shows the synoptic conditions at 1100 LST (UTC + 9 h) associated with the precipitation event. At the 500-hPa level (Fig. 1a), a trough is located northwest of the Korean Peninsula with a pronounced southward protrusion of cold air. At the 850-hPa level (Fig. 1b), a low located north of the Korean Peninsula is evident. The center of the 850-hPa low ($\sim 125^{\circ}\text{E}$) is located east of the axis of the 500-hPa trough ($\sim 123^{\circ}\text{E}$), which indicates a westward-tilted low-pressure system. Strong low-level westerly–northwesterly winds ($\sim 18 \text{ m s}^{-1}$) bring cold air to the SMA (green box in Fig. 1b), which is associated with the passage of the cold front. The field of radar reflectivity at 1130 LST in the SMA is presented in Fig. 2a. Strong echo is aligned in the north-northeast-south-southwest direction in the SMA, indicating a narrow cold-frontal rainband accompanied by limited stratiform precipitation.

Together with the cold front, this cold-frontal precipitation system passes over the SMA from the west to the east during $\sim 1000\text{--}1230$ LST.

2.2. Model description and experimental design

The Weather Research and Forecasting (WRF) model version 4.1.3 (Skamarock et al., 2019) is used to simulate this precipitation event. Three one-way nested domains with horizontal grid spacings of 9, 3, and 1 km are employed (Fig. 3a). Total 50 vertical layers are used, with 10 layers being below $z = 2 \text{ km AGL}$. The vertical grid spacing increases with height from 122 to 448 m. The initial and lateral boundary conditions are given by the European Centre for Medium-Range Weather Forecasts Reanalysis version 5 (ERA5) data (Hersbach et al., 2020) whose temporal and spatial resolutions are 1 h and 0.25° , respectively. The land use/land cover (LULC) distribution at the surface is set in the SMA using the LULC map constructed by Ryu and Baik (2013) based on the geographic information system data from the Korea Ministry of Environment (Fig. 3c). The LULC distribution outside of the SMA is set based on the Moderate Resolution Imaging Spectroradiometer (MODIS) data.

The following physics parameterization options are used for simulations: the Dudhia shortwave radiation scheme (Dudhia, 1989), the Rapid Radiative Transfer Model (RRTM) longwave radiation scheme (Mlawer et al., 1997), the University of Washington planetary boundary layer scheme (Bretherton and Park, 2009), the revised MM5 surface layer scheme (Jiménez et al., 2012), and the unified Noah land surface model (Tewari et al., 2004). The Kain–Fritsch scheme is used for cumulus parameterization only in the outermost domain (Kain, 2004). For urban physics parameterization, the Seoul National University Urban Canopy Model (SNUUCM; Ryu et al., 2011) is employed. The SNUUCM, a single-layer urban canopy model, calculates important physical processes in urban canyon such as the exchanges of turbulent energy between built-up surfaces (i.e., roof, two walls, and road) and the adjacent air, heat transfer through subsurface layers, and absorption and reflection of shortwave/longwave radiation at the built-up surfaces. The performance of the SNUUCM has been evaluated by several studies (e.g.,

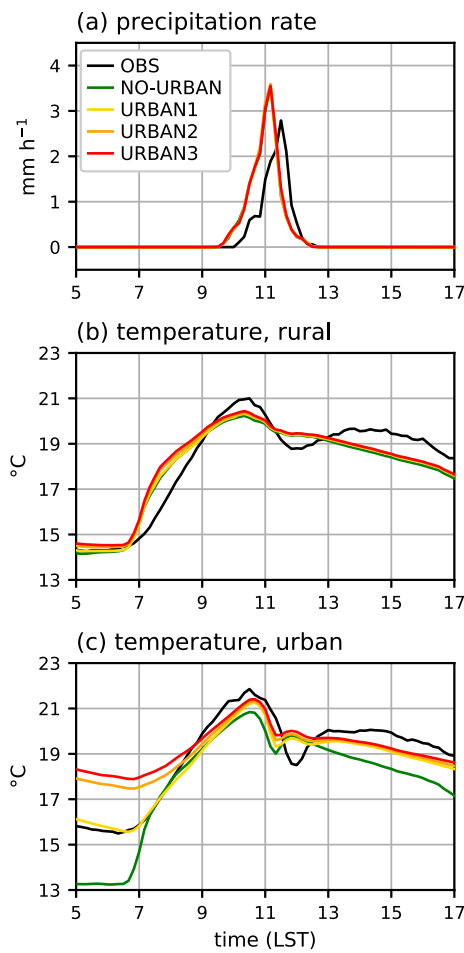


Fig. 4. Time series of (a) precipitation rate averaged over the locations of surface stations and near-surface temperature averaged over the locations of (b) rural and (c) urban stations in the SMA for the observation and for the NO-URBAN, URBAN1, URBAN2, and URBAN3 ensemble simulations.

Ryu et al., 2011, 2012; Ryu and Baik, 2013; Baik et al., 2022) including intercomparison projects (e.g., Grimmond et al., 2010; Lipson et al., 2024).

To examine urban impacts on the precipitation system for different magnitudes of urban forcings, three sets of urban simulations with different pairs of anthropogenic heat intensity and momentum roughness length at the built-up portion of the urban grids in the SMA (pink box in Fig. 3c) are conducted and are named URBAN1, URBAN2, and URBAN3. For the URBAN1 simulations, no anthropogenic heat is considered and the momentum roughness length is set to 1 m. For the URBAN2 and URBAN3 simulations, diurnal-mean anthropogenic heat flux is set to 45 and 90 W m⁻², respectively, with the same temporal change following the diurnal profile of Lee et al. (2009). The anthropogenic heat intensities used for the urban simulations span the range of estimated anthropogenic heat intensity across several cities ($\sim 0\text{--}100 \text{ W m}^{-2}$) (e.g., Sailor and Lu, 2004; Stewart and Kennedy, 2015; Oke et al., 2017). The momentum roughness length for the URBAN2 and URBAN3 simulations is set to 2 and 3 m, respectively. The momentum roughness lengths are determined considering the reported range of momentum roughness length estimated for several cities ($\sim 0.5\text{--}3 \text{ m}$) (e.g., Varquez et al., 2015; Yi et al., 2015; Shen et al., 2022). Except the anthropogenic heat and momentum roughness length in the SMA, other urban parameters are set following Ryu and Baik (2013). For comparisons with the urban simulations, nonurban simulations in which the urban grids in the SMA (pink box in Fig. 3c) are replaced with cropland grids are conducted and named NO-URBAN.

Precipitation simulated in numerical models is highly sensitive to simulation settings (e.g., Kusaka et al., 2009; Forster et al., 2024), which often complicates discerning urban impacts from a comparison between single urban and nonurban simulations. For a reliable examination of urban impacts on precipitation system, 20 ensemble members are produced for each of the simulation sets (i.e., URBAN1, URBAN2, URBAN3, and NO-URBAN) by adopting 5 double-moment microphysics schemes and using 4 simulation periods. The 5 microphysics schemes are the Thompson scheme (Thompson et al., 2008), the Morrison double-moment scheme (Morrison et al., 2009), the WRF double moment 6-class microphysics scheme (Lim and Hong, 2010), the predicted particle properties (P3) scheme (Morrison and Milbrandt, 2015) with the prognostic cloud droplet number concentration, and the ice-spheroids habit model with aspect-ratio evolution (ISHMAEL) scheme (Jensen et al., 2017). For each of the microphysics options, 4 simulations are performed with start times of 0600, 0800, 1000, and 1200 LST 22 September and an end time of 1800 LST 23 September 2023. The 10-min output data on 23 September 2022 are used for analysis.

3. Results and discussion

3.1. Model validation

The field of radar reflectivity at 1110 LST in a single ensemble member of the URBAN1 ensemble simulations is presented in Fig. 2b. The strong echo band oriented in the north-northeast–south-southwest direction with limited stratiform precipitation is well reproduced in the simulation. In some other ensemble members, the reflectivity shows pronounced variability along the band, exhibiting the gap-and-core structure. The time series of precipitation rate averaged over the locations of surface stations in the SMA for the observation and simulations are compared in Fig. 4a. In the observation, the station-averaged precipitation rate peaks at 1130 LST when the precipitation system passes Seoul where many surface stations are concentrated. The precipitation rate in the simulations is overestimated by 33 % and its peak occurs 20 min earlier compared with that in the observation, indicating stronger intensity and earlier arrival of the simulated cold-frontal precipitation system. Given the minimal differences among the four sets of the ensemble simulations, the discrepancies in precipitation intensity and timing between the observation and simulations are likely associated with discrepancies in synoptic systems, rather than those in urban impacts.

The time series of near-surface temperature at the locations of rural and urban stations for the observation and simulations are presented in Fig. 4b and c. The stations in the SMA are classified as urban stations when the stations are located at the urban grids in urban simulations (see Fig. 3c) and otherwise are classified as rural stations. The observed temperature at rural stations increases with time during 0700–1000 LST, as solar heating occurs and the cold front approaches the SMA (Fig. 4b). The temperature peaks at 1030 LST and rapidly drops by 2.2 °C until 1150 LST as the cold front passes the SMA. After the passage, the temperature slightly increases until 1350 LST and then decreases again. The simulated temperature reproduces the general increasing and decreasing tendencies, with deviations of -1 to 2 °C from the observed temperature depending on the time. The peak of the simulated temperature appears 10 min earlier than that of the observed temperature.

The observed temperature at urban stations is, on average, 0.7 °C higher than that at rural stations during 0500–1700 LST, suggesting the UHI impacts (Fig. 4b and c). The simulated temperature at the locations of urban stations tends to be higher in the simulations with stronger urban forcings (Fig. 4c), which is associated with higher surface sensible heat flux; the sensible heat flux averaged over the locations of urban stations during 0500–1700 LST is 23, 117, 144, and 172 W m⁻² in the NO-URBAN, URBAN1, URBAN2, and URBAN3 ensemble simulations, respectively. The magnitude of temperature difference between the four sets of the ensemble simulations at the locations of urban stations is

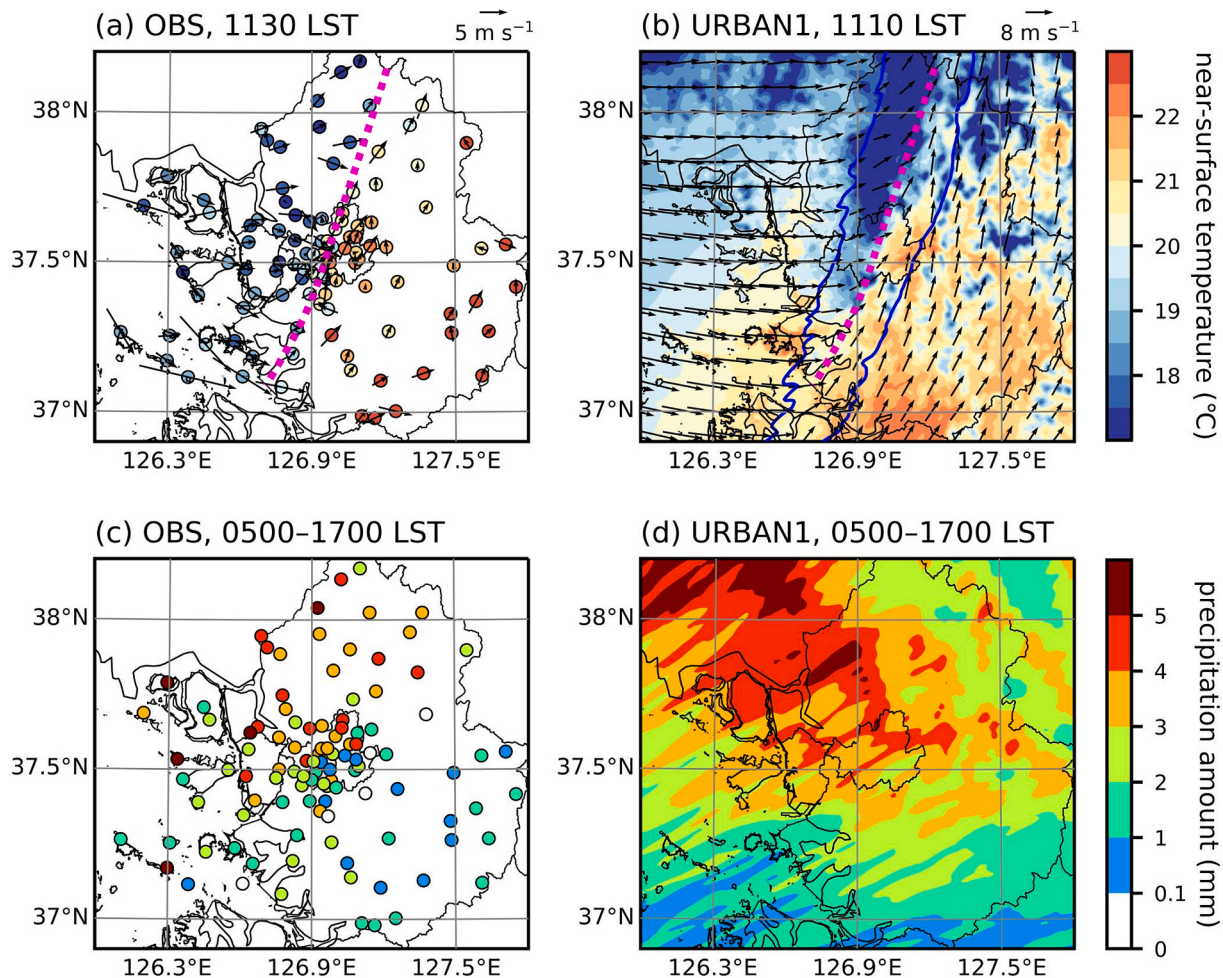


Fig. 5. Spatial distributions of near-surface temperature (shades) and wind vector (arrows) (a) at 1130 LST in the observation and (b) at 1110 LST in the URBAN1 ensemble simulations. The purple dotted line in (a) and (b) indicates a line across which the temperature and wind direction exhibit large contrasts. The precipitation rate of 1 mm h⁻¹ in the URBAN1 ensemble simulations is contoured by blue solid line in (b). Spatial distributions of accumulated precipitation amount during 0500–1700 LST (c) in the observation and (d) in the URBAN1 ensemble simulations. (For interpretation of the references to colour in this figure legend, the reader is referred to the web version of this article.)

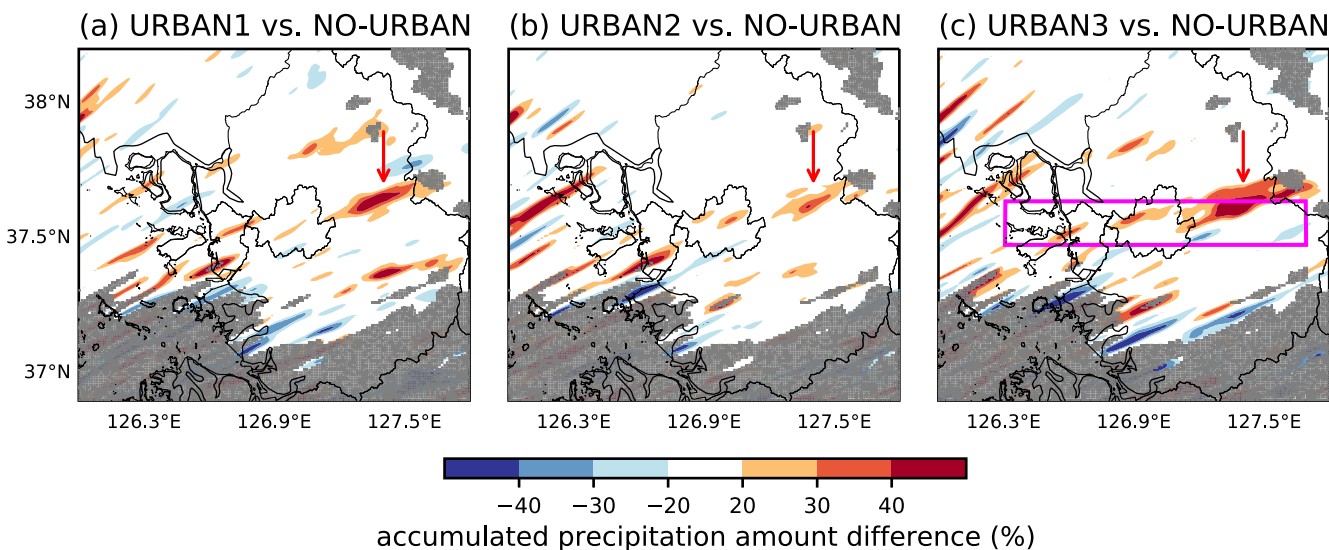


Fig. 6. Fields of relative differences in accumulated precipitation amount between each set of the urban ensemble simulations and the NO-URBAN ensemble simulations during 0500–1700 LST. The areas where the precipitation amount in the NO-URBAN ensemble simulations is smaller than 2 mm are masked by gray shades. The pink box in (c) represents Area 1 which is used for the analysis in Fig. 8. (For interpretation of the references to colour in this figure legend, the reader is referred to the web version of this article.)

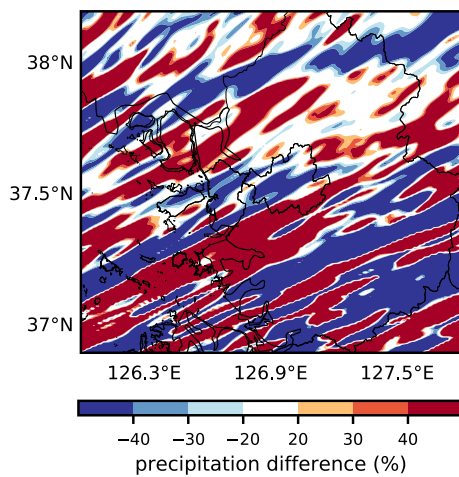


Fig. 7. Field of relative difference in accumulated precipitation amount between a single ensemble member of the URBAN3 ensemble simulations and that of the NO-URBAN ensemble simulations during 0500–1700 LST.

large (~ 5 °C) before 0700 LST, while it is relatively small (< 1 °C) during 0900–1300 LST when the synoptic influences of the frontal system are prominent. The root mean squared error between the observed and simulated urban temperatures during 0500–1700 LST is 1.4, 0.6, 1.0, and 1.2 °C for the NO-URBAN, URBAN1, URBAN2, and URBAN3 ensemble simulations, respectively, indicating that the URBAN1 ensemble simulations exhibit the temperature variation closest to that observed at urban stations. The simulated temperature contrast between the locations of urban and rural stations averaged over 0500–1700 LST is –0.2, 0.5, 0.9, and 1.1 °C for the NO-URBAN, URBAN1, URBAN2, and URBAN3 ensemble simulations, respectively.

The spatial distributions of near-surface temperature and wind behind and ahead of the cold front in the observations and URBAN1 ensemble simulations are illustrated in Fig. 5a and b. Across the purple line oriented in the north-northeast–south-southwest direction, the observed temperature and wind direction exhibit large contrasts (Fig. 5a), indicating the presence of the front. The SMA region west of the purple line is characterized by relatively low temperature (~ 18 °C) and largely westerly-to-northwesterly winds, while that east of the purple line features relatively high temperature (~ 22 °C) and largely southerly-to-southwesterly winds. The simulated temperature west of the purple line is relatively low compared with that east of the purple line and the simulated winds are largely westerly (southerly and southwesterly) west (east) of the purple line (Fig. 5b), generally agreeing with the observation. Meanwhile, the simulations overestimate near-surface wind speed behind and ahead of the front; the simulated near-surface wind speed averaged over the SMA is 7.2 m s^{-1} , being larger than the observed wind speed in the SMA (4.5 m s^{-1}).

Fig. 5c and d shows the spatial distributions of accumulated precipitation amount in the observation and URBAN1 ensemble simulations for this precipitation event. In the observation, the precipitation amount in the northern SMA is relatively large compared with that in the southern SMA (Fig. 5c), as the narrow intense rainband is accompanied by wider stratiform regions in the northern SMA (Fig. 2a). Since the precipitation intensity weakens with time after the landfall, the precipitation amount decreases from the west to the east in the SMA. In the simulations, the spatial variation of accumulated precipitation observed in the SMA is well reproduced although the amount of precipitation is overestimated (Fig. 5d). The overall agreements in the frontal passage (Fig. 4), the distributions of temperature and wind direction around the front (Fig. 5a and b), and the precipitation distribution in the SMA (Fig. 5c and d) between the observation and simulations allow us to examine urban impacts on the cold front and frontal precipitation.

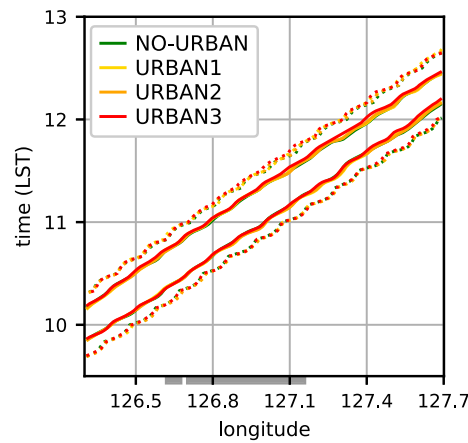


Fig. 8. Longitude–time diagram of precipitation rate (1 mm h^{-1} , dotted; 5 mm h^{-1} , solid) averaged along the y-direction in Area 1 (pink box in Fig. 6c) for the NO-URBAN, URBAN1, URBAN2, and URBAN3 ensemble simulations. The gray boxes in the x-axis indicate the major urban areas in Area 1. (For interpretation of the references to colour in this figure legend, the reader is referred to the web version of this article.)

3.2. Urban impacts on precipitation

The fields of relative differences in accumulated precipitation amount between each set of urban ensemble simulations and the NO-URBAN ensemble simulations are presented in Fig. 6. For the URBAN1 ensemble simulations, a precipitation increase of 20–40 % is found downstorm (i.e., the direction toward which the storm is moving) of Seoul (red arrow). Together with the downstorm increase, several positive and negative anomalies appear in the SMA. For the URBAN2 and URBAN3 ensemble simulations, the downstorm precipitation increase is consistently found at the same location while other positive and negative anomalies appear at different locations. This suggests that the downstorm precipitation increase is attributed to urban impacts while other positive and negative anomalies arise from changes in locations of precipitation cores between the simulations. The downstorm precipitation increase is largest in the URBAN3 ensemble simulations whose urban forcings are strongest. It is notable that the URBAN2 ensemble simulations exhibit less pronounced downstorm precipitation increase compared to the URBAN1 ensemble simulations, which deviates from expectation given the stronger urban forcings in the URBAN2 ensemble simulations. This will be explained in the next subsection where urban impacts on the cold-frontal system are investigated.

The precipitation enhancement downstorm of Seoul due to urban impacts is hard to be discerned by a comparison between single urban and nonurban simulations. Fig. 7 shows the field of relative difference in accumulated precipitation amount between a single ensemble member of the URBAN3 ensemble simulations and the corresponding member of the NO-URBAN ensemble simulations. This ensemble member of the URBAN3 ensemble simulations is one of the best-performing members, having the smallest root mean squared error of accumulated precipitation amount among all members of the URBAN3 ensemble simulations. Streaks of positive and negative anomalies dominate the precipitation difference pattern, obscuring the downstorm precipitation increase due to urban impacts. These streaks result from different locations of precipitation cores along the rainband in the two simulations. The dominance of the anomalies arising from the different locations of precipitation cores is consistently found in comparisons between other single urban and nonurban simulations, regardless of their performances in precipitation simulation (not shown). The comparison between Figs. 6c and 7 shows that the ensemble approach, though not perfect, effectively reduces the magnitude of precipitation anomalies irrelevant to urban impacts, revealing the precipitation increase due to urban

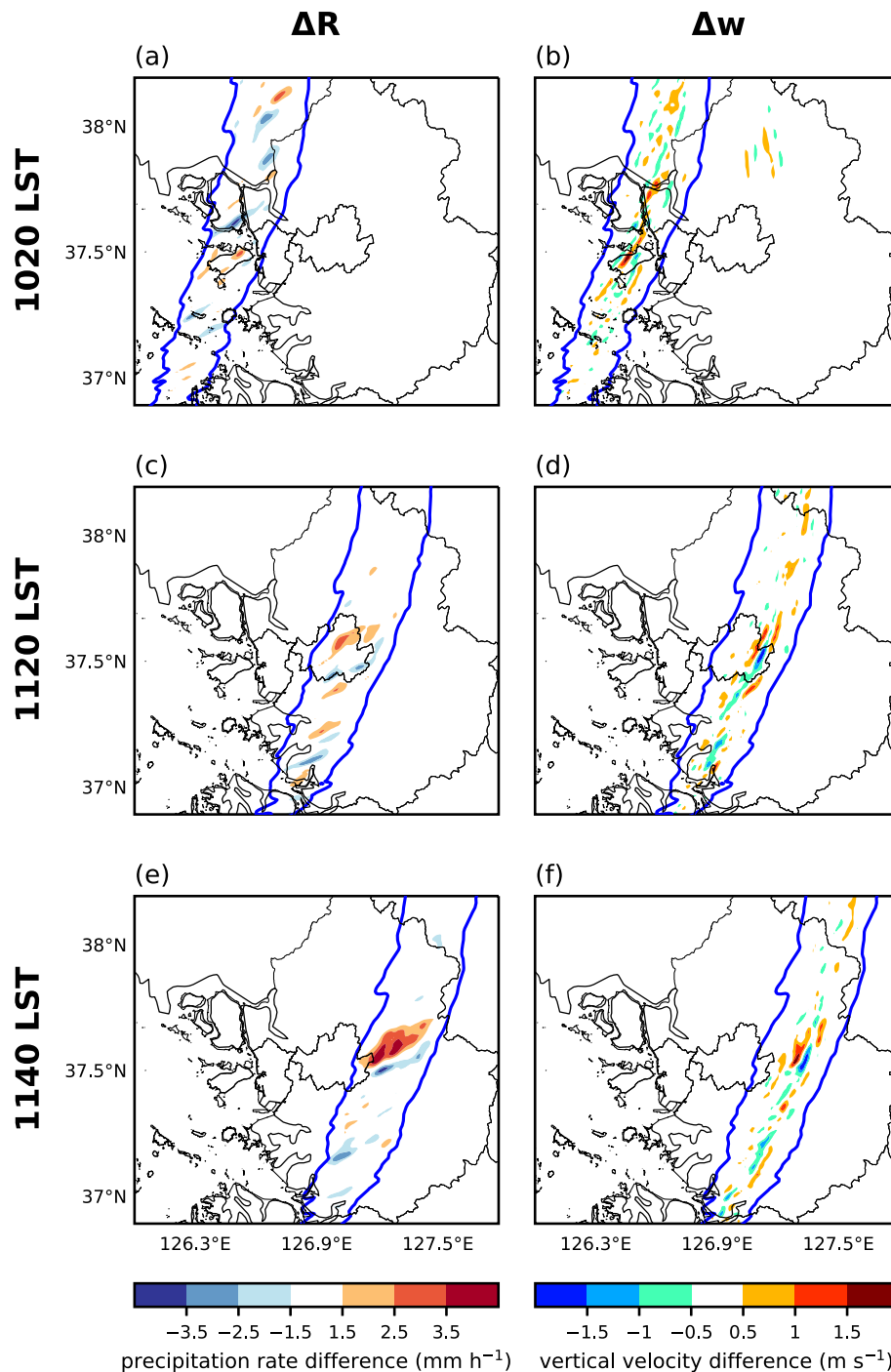


Fig. 9. Fields of differences in (a, c, e) precipitation rate (shades) and (b, d, f) vertical velocity at $z = 1.5 \text{ km MSL}$ between the URBAN3 and NO-URBAN ensemble simulations at (a, b) 1020, (c, d) 1120, and (e, f) 1140 LST. The precipitation rate of 1 mm h^{-1} in the URBAN3 ensemble simulations is contoured by blue lines. (For interpretation of the references to colour in this figure legend, the reader is referred to the web version of this article.)

impacts. This exemplifies an important role of ensemble simulations in examining urban impacts on highly-organized or strongly-forced precipitation systems that have large heterogeneity of precipitation intensity.

Urban impacts on the moving speed of the precipitation system are shown in Fig. 8 which presents the longitude-time diagram of precipitation rate averaged along the y -direction in Area 1 for all sets of the ensemble simulations. The locations of major urban areas in Area 1 are marked by gray boxes in the x -axis. The location of the precipitation system is almost identical for all sets of the ensemble simulations before passing the major urban areas. After the passage, the precipitation

system in the urban ensemble simulations falls behind that in the NO-URBAN ensemble simulations but the delay is marginal; the delay is at best ~ 4 min in the URBAN 3 ensemble simulations. This shows that urban impacts on the moving speed of the cold-frontal precipitation system are insignificant for this event. Since the URBAN3 ensemble simulations exhibit the largest urban impact on precipitation (Figs. 6 and 8) with the strongest urban forcings, the results of the URBAN3 ensemble simulations are mainly used to show urban impacts in the subsequent figures.

The precipitation increase downstorm of Seoul is associated with the changes in frontal updraft and the enhancement of precipitation

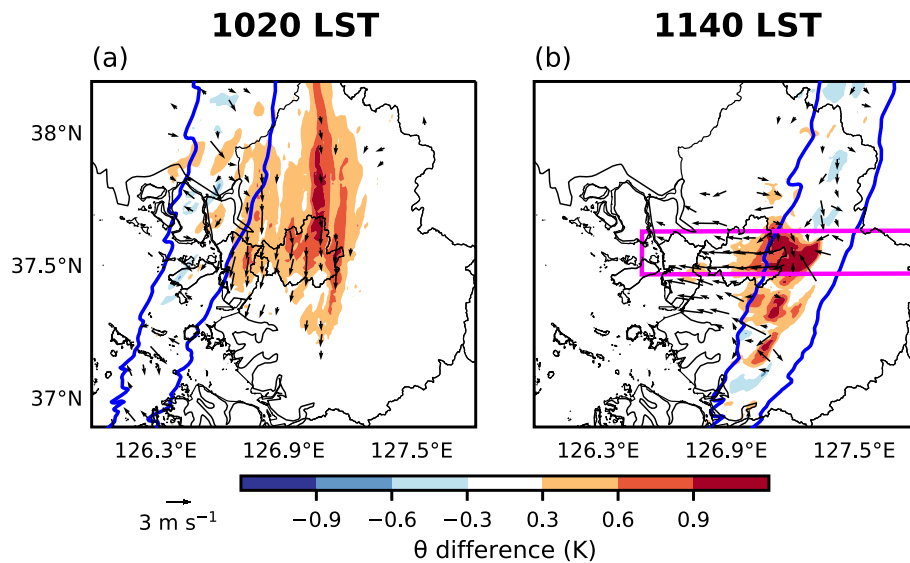


Fig. 10. Fields of differences in potential temperature (shades) and wind vector (arrows, $> 1 \text{ m s}^{-1}$) at the lowest model level between the URBAN3 and NO-URBAN ensemble simulations at (a) 1020 and (b) 1140 LST. The precipitation rate of 1 mm h^{-1} in the URBAN3 ensemble simulations is contoured by blue lines. The pink box in (b) represents Area 2 which is used for the analysis in Figs. 11–14. (For interpretation of the references to colour in this figure legend, the reader is referred to the web version of this article.)

intensity. Fig. 9 shows the fields of differences in precipitation rate and vertical velocity at $z = 1.5 \text{ km}$ MSL between the URBAN3 and NO-URBAN ensemble simulations at different times. The contour for precipitation rate of 1 mm h^{-1} in the URBAN3 ensemble simulations is plotted. At 1020 LST, the precipitation system approaches Seoul (Fig. 9a and b). Some positive and negative anomalies of precipitation rate and vertical velocity are found even before the system passes the urban areas in the SMA, being associated with pre-existing differences in locations of precipitation cores. At 1120 LST, the precipitation system is passing over Seoul (Fig. 9c and d). A weak enhancement of precipitation intensity appears in the rainband segment that passes the urban areas. An enhancement of frontal updraft with intensified downward motion ahead is also found there. After the precipitation system passed over Seoul (Fig. 9e and f), the enhancement of precipitation intensity and strong positive and negative anomalies of vertical velocity become further pronounced. The enhancements of precipitation and frontal updraft persist for about 40 min in the downstorm region. How urban impacts modify the frontal characteristics and enhance the frontal updraft in this precipitation event will be examined in the following subsection.

3.3. Urban impacts on cold-frontal system

Fig. 10 shows the fields of differences in potential temperature and wind vector at the lowest model level between the URBAN3 and NO-URBAN ensemble simulations before and after the frontal passage. The difference of wind vector is plotted only when its magnitude exceeds 1 m s^{-1} . When the cold front approaches Seoul, strong southerly low-level jet ahead of the front advects warm air in urban boundary layer away from the urban areas (Fig. 10a). This significantly reduces the UHI intensity (Fig. 4c). Wind differences directing southward are found over the urban areas, indicating that urban drag decelerates the southerly low-level jet. After the front passes over Seoul, wind differences directing westward appear over the urban areas (Fig. 10b). This shows the deceleration of strong westerly behind the front by urban drag. In addition, strong warm anomaly trailing the cold front is found in and downwind of the urban areas.

To understand urban impacts on the frontal characteristics, the cross-frontal structure of the cold-frontal system and its difference between the URBAN3 and NO-URBAN ensemble simulations at 1140 LST are

presented in Fig. 11. The precipitation system vertically extends up to $z \sim 4.5 \text{ km}$, with a forward-protruding cloud layer ahead of the rainband (Fig. 11a). The frontal updraft is found within narrow intense rainband. The frontal updraft is largely confined below $z \sim 3 \text{ km}$ MSL, consistent with the typical feature of cold-frontal systems (e.g., Clark, 2023; Zou et al., 2023). The environment ahead of the front features strong westerly component at $z \sim 3 \text{ km}$ and weak westerly component near the surface ($< 4 \text{ m s}^{-1}$), with cross-frontal vertical shear over $z = 0\text{--}3 \text{ km}$ reaching $\sim 20 \text{ m s}^{-1}$. Meanwhile, the $0\text{--}3 \text{ km}$ vertical shear behind the front is relatively small ($\sim 8 \text{ m s}^{-1}$) compared with that ahead of the front.

The decrease in low-level wind speed due to urban drag is most prominent over the urban areas and is diminished in the downwind region of the urban areas (Fig. 11b). Meanwhile, the warm anomaly due to urban impacts is most prominent just behind the front, diminishing from the front to the urban center (Fig. 11c). Given that a weakening of cold advection due to urban impacts for a cold-frontal precipitation event was reported (Zhong and Yang, 2015b), this warm anomaly could be associated with the possible weakening of cold advection due to the deceleration or urban heating associated with the enhanced sensible heat flux. To examine urban impacts on the cold advection behind the front, the potential temperature advection is averaged over Region 1 (green box in Fig. 11c) and compared between the two sets of the ensemble simulations. The cold advection is strengthened in the URBAN3 ensemble simulations compared with the NO-URBAN ensemble simulations despite the wind speed decrease, as the horizontal gradient of potential temperature in the urban areas is changed. This suggests that the warm anomaly behind the front in this cold-frontal precipitation event is likely produced by the downwind-adverted warm urban-heated air associated with the UHI impacts, rather than a weakened cold advection due to the urban drag impacts.

Fig. 12 shows the fields of differences in x-directional velocity, vertical velocity, and y-directional vorticity between the URBAN3 and NO-URBAN ensemble simulations at 1140 LST. Since the low-level wind behind the front is largely westerly, the pattern of x-directional velocity difference largely agrees with that of wind speed difference (Figs. 11b and 12a). An exception is the prominent negative anomaly of x-directional velocity at the leading edge of the front (red arrow in Fig. 12a), whose magnitude is much larger than the decrease in the magnitude of total horizontal wind (Fig. 11b). This signifies that a negative anomaly

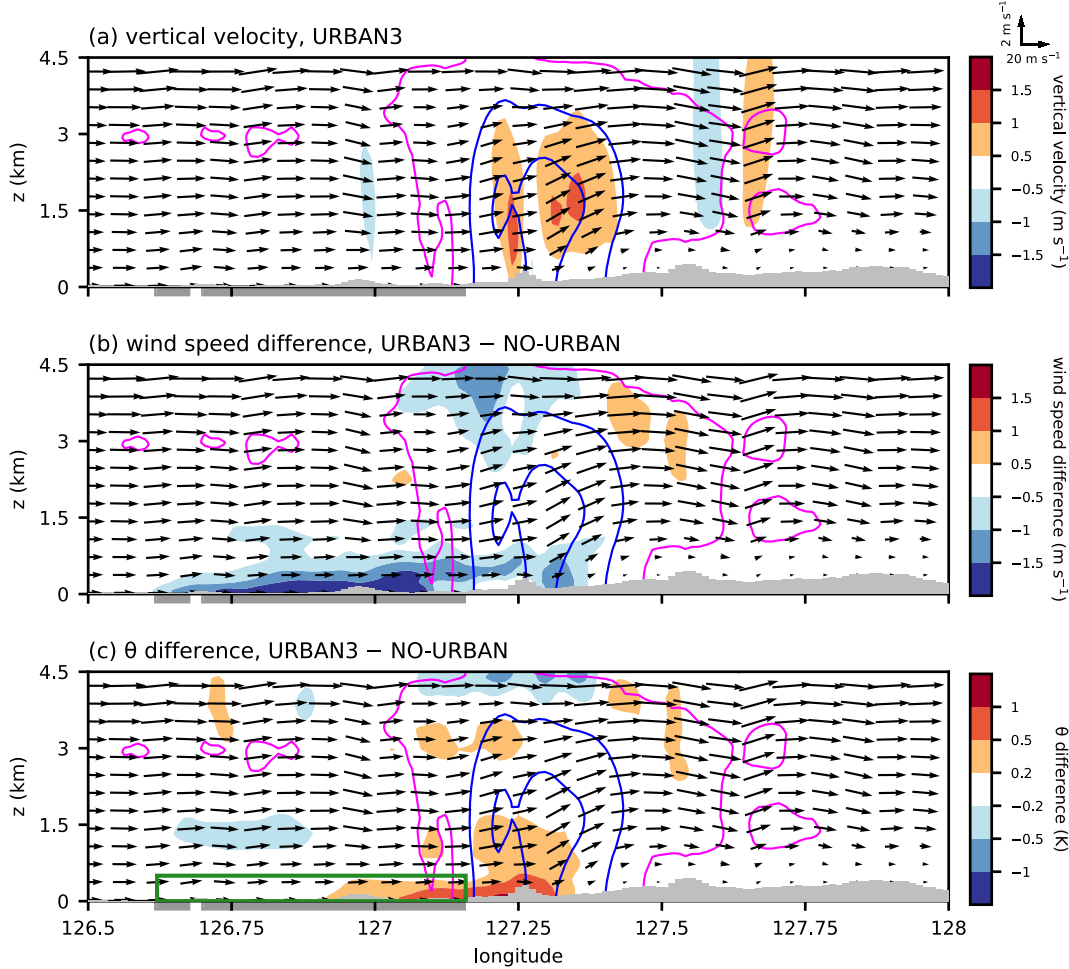


Fig. 11. (a) Fields of vertical velocity (shades), wind vector (arrows), total hydrometeor mixing ratio (pink contours, at 0.01 g kg^{-1}), and rainwater mixing ratio (blue contours, at 0.1 and 0.4 g kg^{-1}) averaged along the y -direction in Area 2 at 1140 LST for the URBAN3 ensemble simulations. (b, c) As in (a), but for differences in (b) wind speed (shades) and (c) potential temperature (shades) between the URBAN3 and NO-URBAN ensemble simulations. The light gray-shaded areas represent the topography in Area 2. The dark gray boxes in the x -axis indicate the major urban areas in Area 2. The green box in (c) represents Region 1 where the potential temperature advection is averaged. (For interpretation of the references to colour in this figure legend, the reader is referred to the web version of this article.)

of x -directional velocity is generated by urban impacts at the leading edge of the front. A positive anomaly of x -directional velocity is found at $z \sim 3 \text{ km MSL}$ just above the prominent negative anomaly. At the same location, a pair of pronounced positive and negative anomalies of vertical velocity is present, with the positive anomaly enhancing the frontal updraft (Fig. 12b). These pairs of positive and negative anomalies of x -directional and vertical velocities indicate that urban impacts increase the y -directional vorticity at the leading edge of the cold front (red arrow in Fig. 12c). The vorticity is increased over the urban areas at the low levels as well, due to the deceleration of low-level westerly by urban drag.

To investigate why the vorticity is generated by urban impacts at the leading edge of the cold front, the urban-induced difference in each term of y -directional vorticity equation is examined. The y -directional vorticity equation derived from the governing equations of momentum in the WRF model is as follows:

$$\frac{D\eta}{Dt} = -\eta(\nabla \cdot \mathbf{u}) + (\boldsymbol{\omega} \cdot \nabla)v + \frac{1}{\rho^2} \left(\frac{\partial p}{\partial z} \frac{\partial p}{\partial x} - \frac{\partial p}{\partial x} \frac{\partial p}{\partial z} \right) + F_{res}, \quad (1)$$

where η is the y -directional vorticity, $\mathbf{u} = (u, v, w)$ is the velocity vector, $\boldsymbol{\omega} = (\xi, \eta, \zeta)$ is the vorticity vector, ρ is the density of air including hydrometeors, and p is the pressure. Here, the term on the left-hand side of Eq. (1) is the total derivative of y -directional vorticity. The first, second, third, and fourth terms on the right-hand side of Eq. (1) are the

stretching term, tilting term, baroclinic term, and residual term, respectively. The residual term includes the vorticity change rates due to the Coriolis and curvature effects, boundary-layer mixing, diffusion, and surface forcing. ρ in the baroclinic term is a function of potential temperature, water vapor mixing ratio, total hydrometeor mixing ratio, and pressure (Skamarock et al., 2019). This means that the gradients of potential temperature, water vapor mixing ratio, total hydrometeor mixing ratio, and pressure contribute to the baroclinic term. All the terms in Eq. (1) are calculated for each ensemble member and then averaged over the ensemble members for analysis.

Fig. 13 shows the fields of differences in the total derivative of y -directional vorticity, stretching and tilting terms, residual term, and baroclinic term between the URBAN3 and NO-URBAN ensemble simulations at 1140 LST. A positive anomaly of the total derivative is found at the leading edge of the cold front (green box) (Fig. 13a), which is responsible for the forefront vorticity increase (Fig. 13c). While the stretching and tilting terms and residual term also affect the total derivative, their net contributions to the positive anomaly of the total derivative at the leading edge of the front are negligible (Fig. 13b and c). The baroclinic term is responsible for the positive anomaly of the total derivative (Fig. 13d). The dominant role of baroclinic term on the positive anomaly of the total derivative at the leading edge of the front persists for the period during which the enhancement of precipitation intensity occurs downstorm of the urban areas. This urban-induced

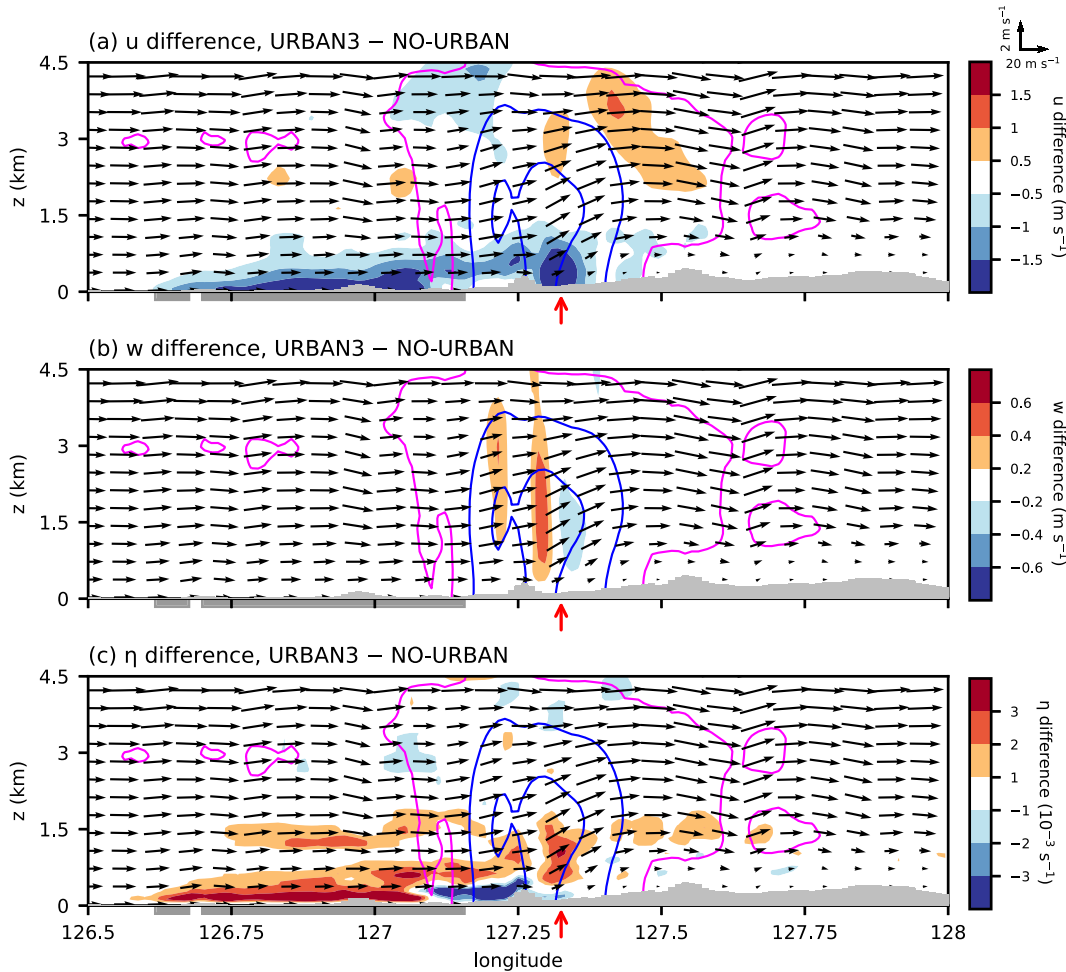


Fig. 12. As in Fig. 11b, but for the differences in (a) x-directional velocity (shades), (b) vertical velocity (shades), and (c) y-directional vorticity (shades) between the URBAN3 and NO-URBAN ensemble simulations.

increase in the baroclinic term is largely attributed to the decrease in x -directional gradient of potential temperature which is associated with the trailing warm anomaly (Fig. 11c).

The UHI-induced increases in y -directional vorticity are responsible for the enhancements of updraft and precipitation in the URBAN1 and URBAN2 ensemble simulations as well as in the URBAN3 ensemble simulations. Although the magnitude of trailing warm anomaly and the increase in baroclinic term exhibit increasing tendencies with strengthening urban forcing (not shown), the downstorm precipitation enhancement is weaker in the URBAN2 ensemble simulations than in the URBAN1 ensemble simulations (Fig. 6a and b). This is associated with the location at which the updraft enhancement occurs. The fields of differences in vertical velocity between each set of the urban ensemble simulations and the NO-URBAN ensemble simulations at the time of the most prominent updraft enhancement are presented in Fig. 14, to compare the main location of updraft enhancement between the three sets of the urban ensemble simulations. While the updraft enhancement occurs well within the frontal updraft in the URBAN1 and URBAN3 ensemble simulations (Fig. 14a and c), it occurs slightly ahead of the frontal updraft in the URBAN2 ensemble simulations (Fig. 14b). This suggests that the urban-induced updraft enhancement needs to be collocated with the frontal updraft for the prominent frontal precipitation enhancement.

For the cold front case examined in this study, the UHI impacts lead to the trailing warm anomaly behind the cold front, increasing the cross-

frontal vorticity and enhancing the frontal updraft intensity. Previous studies using observations and simulations (Parsons, 1992; Yu and Smull, 2000; Jorgensen et al., 2003) suggested that frontal updraft of cold front can be understood to some extent based on the squall-line theory (Rotunno et al., 1988) which explains gust-frontal updraft intensity using the balance between horizontal vorticity associated with the environmental wind shear and horizontal vorticity baroclinically generated by the density gradient. This implies that whether the urban-induced increase in y -directional vorticity enhances frontal updraft and precipitation or not may depend on the specific conditions of the given cold front such as environmental shear and cross-frontal temperature gradient. Further investigation of urban impacts on cold-frontal precipitation system for various cases of cold front is needed.

4. Summary and conclusions

This study examined urban impacts on a cold-frontal precipitation system passing over the SMA using ensemble simulations. The urban impacts on cold front and accompanying precipitation system for the examined cold front case are summarized in Fig. 15. After the cold front passes over the urban areas, urban drag decelerates the strong westerlies behind the front. The warm urban air heated by the large urban sensible heat is advected downwind, increasing potential temperature behind the front. This decreases the cross-frontal gradient of potential temperature at the leading edge of the front and therefore increases baroclinic

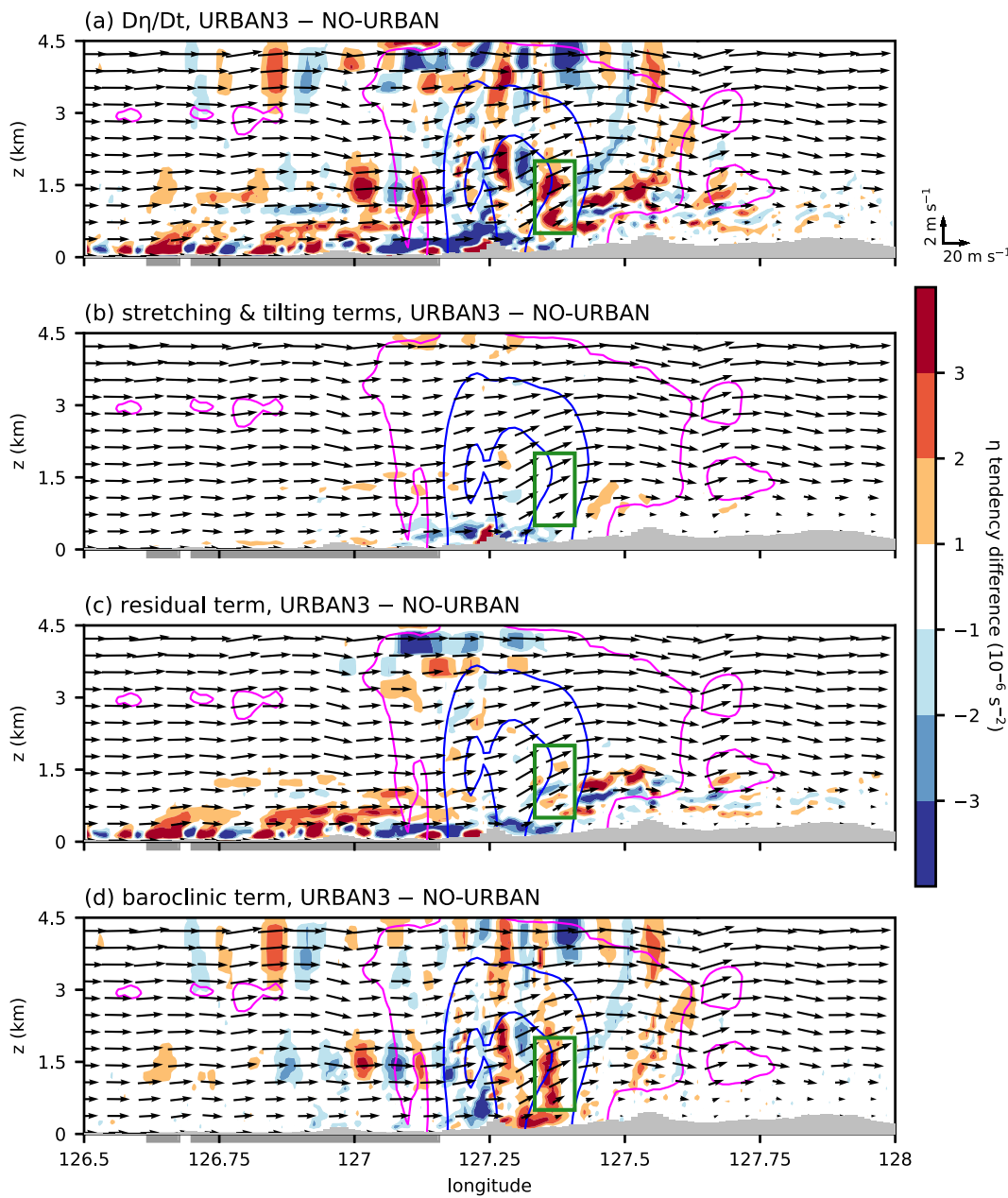


Fig. 13. As in Fig. 11b, but for the differences in (a) the total derivative of y-directional vorticity, (b) stretching and tilting terms, (c) residual term, and (d) baroclinic term in the y-directional vorticity equation between the URBAN3 and NO-URBAN ensemble simulations.

generation of cross-frontal vorticity, leading to the enhancements of frontal updraft intensity and precipitation downstorm of the urban areas.

The downstorm precipitation enhancements revealed from the comparisons between the urban and nonurban ensemble simulations were difficult to be detected by comparing an urban simulation with a nonurban simulation. This is because the magnitude of urban-induced precipitation enhancements is smaller than the along-frontal variability in precipitation intensity associated with precipitation cores and gaps whose locations are differently simulated for each simulation run. This result implies inherent difficulties in examining urban modification of precipitation systems having a large spatial heterogeneity of precipitation intensity, through a comparison between single pair of urban and nonurban simulations or an examination of radar reflectivity evolution observed in single precipitation event.

This study suggested that for the examined cold-front precipitation event, the UHI can enhance frontal updraft by baroclinically generating

cross-frontal vorticity. Further investigation is needed to understand whether this urban impact frequently occurs, through simulations of similar cold-frontal precipitation events in other cities and/or observational analysis using composite of multiple events. In addition to the anthropogenic heat intensity and momentum roughness length examined in this study, the urban size is another characteristic of cities important to urban impact. Future investigation differing urban size would help to characterize the expected intensity and spatial extent of urban impacts for a range of cities with different sizes. The cold-frontal precipitation system examined in this study is accompanied by limited regions of stratiform precipitation. Meanwhile, in some other cold-frontal precipitation events (e.g., Zou et al., 2023; Zhang and Schultz, 2024), stratiform precipitation from wide cold-frontal rainband also accounts for significant portion of total precipitation amount. Further investigation of urban impacts on this stratiform precipitation can contribute to a comprehensive understanding of urban impacts on cold-frontal precipitation systems.

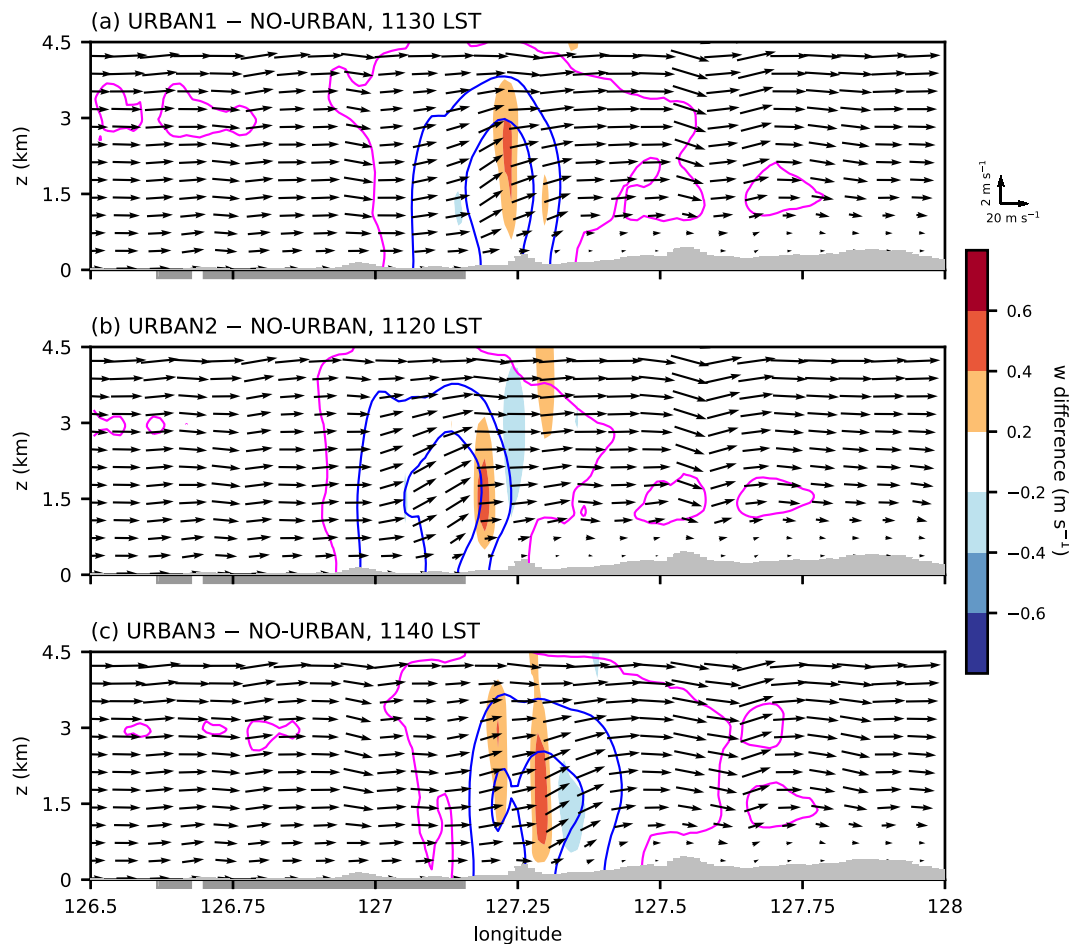


Fig. 14. As in Fig. 12b, but for the (a) URBAN1, (b) URBAN2, and (c) URBAN3 ensemble simulations at the time when the updraft enhancement downstorm of the urban areas is most pronounced in each set of the urban ensemble simulations.

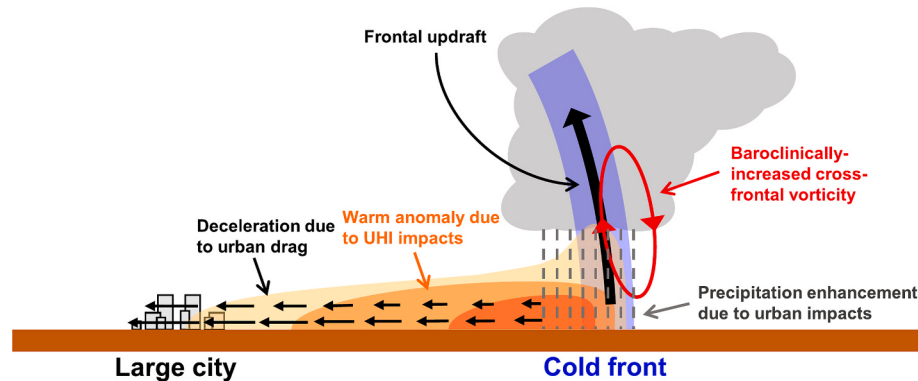


Fig. 15. Schematic diagram that depicts the urban impacts on cold-frontal system and its associated precipitation for the cold-frontal precipitation event examined in this study.

CRediT authorship contribution statement

Seong-Ho Hong: Visualization, Investigation, Formal analysis, Writing – original draft. **Jong-Jin Baik:** Supervision, Formal analysis, Conceptualization, Writing – review & editing.

Declaration of competing interest

The authors declare that they have no known competing financial interests or personal relationships that could have appeared to influence

the work reported in this paper.

Acknowledgements

The authors are grateful to two anonymous reviewers who provided valuable comments on this work. This work was supported by the National Research Foundation of Korea under grants 2021R1A2C1007044 and RS-2025-00562044.

Data availability

The data that support the findings of this study are available from the corresponding author upon reasonable request.

References

- Andrey, J., Mills, B., Leahy, M., Suggett, J., 2003. Weather as a chronic hazard for road transportation in Canadian cities. *Nat. Hazards* 28, 319–343.
- Baik, J.-J., Kim, Y.-H., Chun, H.-Y., 2001. Dry and moist convection forced by an urban heat island. *J. Appl. Meteorol.* 40, 1462–1475.
- Baik, J.-J., Lim, H., Han, B.-S., Jin, H.-G., 2022. Cool-roof effects on thermal and wind environments during heat waves: a case modeling study in Seoul, South Korea. *Urban Clim.* 41, 101044.
- Bretherton, C.S., Park, S., 2009. A new moist turbulence parameterization in the Community Atmosphere Model. *J. Clim.* 22, 3422–3448.
- Changnon, S.A., Huff, F.A., Schickelanz, P.T., Vogel, J.L., 1977. Summary of METROMEX, Volume 1: Weather Anomalies and Impacts. Illinois State Water Survey, Urbana.
- Chung, Y., 2012. Assessment of non-recurrent congestion caused by precipitation using archived weather and traffic flow data. *Transp. Policy* 19, 167–173.
- Clark, M.R., 2023. Synoptic-scale and mesoscale controls for tornadogenesis on cold fronts: a tornadic cold front in amplifying northwesterly flow. *Q. J. R. Meteorol. Soc.* 149, 1407–1434.
- Dąbrowska, J., Orellana, A.E.M., Kilian, W., Moryl, A., Cielecka, N., Michalowska, K., Policht-Latawiec, A., Michalski, A., Bednarek, A., Wióka, A., 2023. Between flood and drought: how cities are facing water surplus and scarcity. *J. Environ. Manag.* 345, 118557.
- Doan, Q.-V., Dipankar, A., Simón-Moral, A., Sanchez, C., Prasanna, V., Roth, M., Huang, X.-Y., 2021. Urban-induced modifications to the diurnal cycle of rainfall over a tropical city. *Q. J. R. Meteorol. Soc.* 147, 1189–1201.
- Dudhia, J., 1989. Numerical study of convection observed during the Winter Monsoon Experiment using a mesoscale two-dimensional model. *J. Atmos. Sci.* 46, 3077–3107.
- Fan, J., Zhang, Y., Li, Z., Hu, J., Rosenfeld, D., 2020. Urbanization-induced land and aerosol impacts on sea-breeze circulation and convective precipitation. *Atmos. Chem. Phys.* 20, 14163–14182.
- Forster, A., Augros, C., Masson, V., 2024. Urban influence on convective precipitation in the Paris region: hectometric ensemble simulations in a case study. *Q. J. R. Meteorol. Soc.* 150, 3028–3051.
- Gaffen, D., Bornstein, R.D., 1988. Case study of urban interactions with a synoptic scale cold front. *Meteorol. Atmos. Phys.* 38, 185–194.
- Gimeno, L., Nieto, R., Vázquez, M., Lavers, D.A., 2014. Atmospheric rivers: a mini-review. *Front. Earth Sci.* 2, 2.
- Grimmond, C.S.B., Blackett, M., Best, M.J., Barlow, J., Baik, J.-J., Belcher, S.E., Bohnenstengel, S.I., Calmet, I., Chen, F., Dandou, A., Fortuniak, K., Gouveia, M.L., Hamdi, R., Hendry, M., Kawai, T., Kawamoto, Y., Kondo, H., Krayenhoff, E.S., Lee, S.-H., Loridan, T., Martilli, A., Masson, V., Miao, S., Oleson, K., Pigeon, G., Porson, A., Ryu, Y.-H., Salamanca, F., Shashua-Bar, L., Steeneveld, G.-J., Tombrou, M., Voogt, J., Young, D., Zhang, N., 2010. The international urban energy balance models comparison project: first results from phase 1. *J. Appl. Meteorol. Climatol.* 49, 1268–1292.
- Haberle, A.M., Ashley, W.S., 2019. A radar-based climatology of mesoscale convective systems in the United States. *J. Clim.* 32, 1591–1606.
- Han, J.-Y., Baik, J.-J., 2008. A theoretical and numerical study of urban heat island-induced circulation and convection. *J. Atmos. Sci.* 65, 1859–1877.
- Han, J.-Y., Baik, J.-J., Lee, H., 2014. Urban impacts on precipitation. *Asia-Pac. J. Atmos. Sci.* 50, 17–30.
- Hersbach, H., Bell, B., Berrisford, P., Hirahara, S., Horányi, A., Muñoz-Sabater, J., Nicolas, J., Peubey, C., Radu, R., Schepers, D., Simmons, A., Soci, C., Abdalla, S., Abellán, X., Balsamo, G., Bechtold, P., Biavati, G., Bidlot, J., Bonavita, M., Chiara, G., Dahlgren, P., Dee, D., Diamantakis, M., Dragani, R., Flemming, J., Forbes, R., Fuentes, M., Geer, A., Haimberger, L., Healy, S., Hogan, R.J., Hölm, E., Janisková, M., Keeley, S., Laloyaux, P., Lopez, P., Lupu, C., Radnoti, G., Rosnay, P.D., Rozum, I., Vamborg, F., Villaume, S., Thépaut, J.-N., 2020. The ERA5 global reanalysis. *Q. J. R. Meteorol. Soc.* 146, 1999–2049.
- Houze, R.A., 2014. Cloud Dynamics, second ed. Academic Press, Oxford.
- Hu, H., Feng, Z., Leung, L.-Y.R., 2021. Linking flood frequency with mesoscale convective systems in the US. *Geophys. Res. Lett.* 48, e2021GL092546.
- IPCC, 2023. Climate Change 2023: Synthesis Report. Intergovernmental Panel on Climate Change, Geneva.
- Jensen, A.A., Harrington, J.Y., Morrison, H., Milbrandt, J.A., 2017. Predicting ice shape evolution in a bulk microphysics model. *J. Atmos. Sci.* 74, 2081–2104.
- Jiménez, P.A., Dudhia, J., González-Rouco, J.F., Navarro, J., Montávez, J.P., García-Bustamante, E., 2012. A revised scheme for the WRF surface layer formulation. *Mon. Weather Rev.* 140, 898–918.
- Jorgensen, D.P., Pu, Z., Persson, P.O.G., Tao, W.-K., 2003. Variations associated with cores and gaps of a Pacific narrow cold frontal rainband. *Mon. Weather Rev.* 131, 2705–2729.
- Kain, J.S., 2004. The Kain–Fritsch convective parameterization: an update. *J. Appl. Meteorol.* 43, 170–181.
- Kusaka, H., Kimura, F., Nawata, K., Hanyu, T., Miya, Y., 2009. The chink in the armor: Questioning the reliability of conventional sensitivity experiments in determining urban effects on precipitation patterns. In: 7th International Conference on Urban Climate. International Association for Urban Climate.
- Kusaka, H., Nishi, A., Mizunari, M., Yokoyama, H., 2019. Urban impacts on the spatiotemporal pattern of short-duration convective precipitation in a coastal city adjacent to a mountain range. *Q. J. R. Meteorol. Soc.* 145, 2237–2254.
- Lee, S.-H., Song, C.-K., Baik, J.-J., Park, S.-U., 2009. Estimation of anthropogenic heat emission in the Gyeong-in region of Korea. *Theor. Appl. Climatol.* 96, 291–303.
- Li, H., Cui, X., Zhang, D.-L., 2017. Sensitivity of the initiation of an isolated thunderstorm over the Beijing metropolitan region to urbanization, terrain morphology and cold outflows. *Q. J. R. Meteorol. Soc.* 143, 3153–3164.
- Lim, K.-S.S., Hong, S.-Y., 2010. Development of an effective double-moment cloud microphysics scheme with prognostic cloud condensation nuclei (CCN) for weather and climate models. *Mon. Weather Rev.* 138, 1587–1612.
- Lipson, M.J., Grimmond, S., Best, M., Abramowitz, G., Coutts, A., Tapper, N., Baik, J.-J., Beyers, M., Blunn, L., Boussetta, S., Bou-Zeid, E., Kauwe, M.G.D., Munck, C.D., Demuzere, M., Faticchi, S., Fortuniak, K., Han, B.-S., Hendry, M.A., Kikegawa, Y., Kondo, H., Lee, D.-I., Lee, S.-H., Lemonsu, A., Machado, T., Manoli, G., Martilli, A., Masson, V., McNorton, J., Meili, N., Meyer, D., Nice, K.A., Oleson, K.W., Park, S.-B., Roth, M., Schoetter, R., Simón-Moral, A., Steeneveld, G.-J., Sun, T., Takane, Y., Thatcher, M., Tsirngakis, A., Varentsov, M., Wang, C., Wang, Z.-H., Pitman, A.J., 2024. Evaluation of 30 urban land surface models in the Urban-PLUMBER project: phase 1 results. *Q. J. R. Meteorol. Soc.* 150, 126–169.
- Liu, J., Niyogi, D., 2019. Meta-analysis of urbanization impact on rainfall modification. *Sci. Rep.* 9, 7301.
- Loose, T., Bornstein, R.D., 1977. Observations of mesoscale effects on frontal movement through an urban area. *Mon. Weather Rev.* 105, 563–571.
- Mak, M., Lu, Y., Deng, Y., 2017. Two issues concerning surface frontogenesis. *J. Atmos. Sci.* 74, 2967–2987.
- Markowski, P., Richardson, Y., 2010. Mesoscale Meteorology in Midlatitudes. Wiley-Blackwell, West Sussex.
- Mlawer, E.J., Taubman, S.J., Brown, P.D., Iacono, M.J., Clough, S.A., 1997. Radiative transfer for inhomogeneous atmospheres: RRTM, a validated correlated-k model for the longwave. *J. Geophys. Res.* 102, 16663–16682.
- MOIS, 2024. 2022 Disaster Annual Report. Ministry of the Interior and Safety, Sejong City.
- Morrison, H., Milbrandt, J.A., 2015. Parameterization of cloud microphysics based on the prediction of bulk ice particle properties. Part I: scheme description and idealized tests. *J. Atmos. Sci.* 72, 287–311.
- Morrison, H., Thompson, G., Tatarkii, V., 2009. Impact of cloud microphysics on the development of trailing stratiform precipitation in a simulated squall line: comparison of one- and two-moment schemes. *Mon. Weather Rev.* 137, 991–1007.
- NCEI, 2025. U.S. Billion-Dollar Weather and Climate Disasters. <https://www.ncei.noaa.gov/access/billions/state-summary/US> (accessed 1 March 2025).
- Norris, J., Vaughan, G., Schultz, D.M., 2017. Variability of precipitation along cold fronts in idealized baroclinic waves. *Mon. Weather Rev.* 145, 2971–2992.
- Oke, T.R., Mills, G., Christen, A., Voogt, J.A., 2017. Urban Climates. Cambridge University Press, Cambridge.
- Parsons, D.B., 1992. An explanation for intense frontal updrafts and narrow cold-frontal rainbands. *J. Atmos. Sci.* 49, 1810–1825.
- Qian, Y., Chakraborty, T.C., Li, J., Li, D., He, C., Sarangi, C., Chen, F., Yang, X., Leung, L.R., 2022. Urbanization impact on regional climate and extreme weather: current understanding, uncertainties, and future research directions. *Adv. Atmos. Sci.* 39, 819–860.
- Ralph, F.M., Neiman, P.J., Wick, G.A., 2004. Satellite and CALJET aircraft observations of atmospheric rivers over the eastern North Pacific Ocean during the winter of 1997/98. *Mon. Weather Rev.* 132, 1721–1745.
- Ralph, F.M., Rutz, J.J., Cordeira, J.M., Dettinger, M., Anderson, M., Reynolds, D., Schick, L.J., Smallcomb, C., 2019. A scale to characterize the strength and impacts of atmospheric rivers. *Bull. Am. Meteorol. Soc.* 100, 269–289.
- Rappaport, E.N., 2014. Fatalities in the United States from Atlantic tropical cyclones: new data and interpretation. *Bull. Am. Meteorol. Soc.* 95, 341–346.
- Reames, L.J., Stensrud, D.J., 2018. Influence of a Great Plains urban environment on a simulated supercell. *Mon. Weather Rev.* 146, 1437–1462.
- Rotunno, R., Klemp, J.B., Weisman, M.L., 1988. A theory for strong, long-lived squall lines. *J. Atmos. Sci.* 45, 463–485.
- Rozoff, C.M., Cotton, W.R., Adegoke, J.O., 2003. Simulation of St. Louis, Missouri, land use impacts on thunderstorms. *J. Appl. Meteorol.* 42, 716–738.
- Rüdistühli, S., Sprenger, M., Leutwyler, D., Schär, C., Wernli, H., 2020. Attribution of precipitation to cyclones and fronts over Europe in a kilometer-scale regional climate simulation. *Weather Clim. Dyn.* 1, 675–699.
- Ryu, Y.-H., Baik, J.-J., 2013. Daytime local circulations and their interactions in the Seoul metropolitan area. *J. Appl. Meteorol. Climatol.* 52, 784–801.
- Ryu, Y.-H., Baik, J.-J., Lee, S.-H., 2011. A new single-layer urban canopy model for use in mesoscale atmospheric models. *J. Appl. Meteorol. Climatol.* 50, 1773–1794.
- Ryu, Y.-H., Baik, J.-J., Lee, S.-H., 2012. Performance comparison of an urban canopy model under different meteorological conditions. *Atmos.-Korea* 22, 429–436.
- Sailor, D.J., Lu, L., 2004. A top-down methodology for developing diurnal and seasonal anthropogenic heating profiles for urban areas. *Atmos. Environ.* 38, 2737–2748.
- Seino, N., Aoyagi, T., Tsuguti, H., 2018. Numerical simulation of urban impact on precipitation in Tokyo: how does urban temperature rise affect precipitation? *Urban Clim.* 23, 8–35.
- Shen, C., Shen, A., Cui, Y., Chen, X., Liu, Y., Fan, Q., Chan, P., Tian, C., Wang, C., Lan, J., Gao, M., Li, X., Wu, J., 2022. Spatializing the roughness length of heterogeneous urban underlying surfaces to improve the WRF simulation-part 1: a review of morphological methods and model evaluation. *Atmos. Environ.* 270, 118874.

- Simón-Moral, A., Dipankar, A., Doan, Q.-V., Sanchez, C., Roth, M., Becker, E., Huang, X.-Y., 2021. Urban intensification of convective rainfall over the Singapore–Johor Bahru region. *Q. J. R. Meteorol. Soc.* 147, 3665–3680.
- Skamarock, W.C., Klemp, J.B., Dudhia, J., Gill, D.O., Liu, Z., Berner, J., Wang, W., Powers, J.G., Duda, M.G., Barker, D.M., Huang, X.-Y., 2019. A Description of the Advanced Research WRF Model Version 4. National Center for Atmospheric Research, Boulder.
- Stewart, I., Kennedy, C., 2015. Estimating anthropogenic heat release from megacities. In: 9th International Conference on Urban Climate Jointly with the 12th Symposium on the Urban Environment. International Association for Urban Climate.
- Sun, X., Luo, Y., Gao, X., Wu, M., Li, M., Huang, L., Zhang, D.-L., Xu, H., 2021. On the localized extreme rainfall over the Great Bay Area in South China with complex topography and strong UHI effects. *Mon. Weather Rev.* 149, 2777–2801.
- Tewari, M., Chen, F., Wang, W., Dudhia, J., LeMone, M.A., Mitchell, K., Ek, M., Gayno, G., Wegiel, J., Cuenca, R.H., 2004. Implementation and verification of the unified Noah land surface model in the WRF model. In: 20th Conference on Weather Analysis and Forecasting/16th Conference on Numerical Weather Prediction. American Meteorological Society.
- Thielen, J., Wobrock, W., Gadian, A., Mestayer, P.G., Creutin, J.-D., 2000. The possible influence of urban surfaces on rainfall development: a sensitivity study in 2D in the meso-γ-scale. *Atmos. Res.* 54, 15–39.
- Thompson, G., Field, P.R., Rasmussen, R.M., Hall, W.D., 2008. Explicit forecasts of winter precipitation using an improved bulk microphysics scheme. Part II: implementation of a new snow parameterization. *Mon. Weather Rev.* 136, 5095–5115.
- Utsumi, N., Kim, H., Seto, S., Kanae, S., Oki, T., 2014. Climatological characteristics of fronts in the western North Pacific based on surface weather charts. *J. Geophys. Res. Atmos.* 119, 9400–9418.
- Varquez, A.C.G., Nakayoshi, M., Kanda, M., 2015. The effects of highly detailed urban roughness parameters on a sea-breeze numerical simulation. *Bound.-Layer Meteorol.* 154, 449–469.
- WMO, 2021. *Atlas of Mortality and Economic Losses from Weather, Climate and Water Extremes (1970–2019)*. World Meteorological Organization, Geneva.
- Yang, L., Smith, J., Niyogi, D., 2019. Urban impacts on extreme monsoon rainfall and flooding in complex terrain. *Geophys. Res. Lett.* 46, 5918–5927.
- Yi, C., Kwon, T.H., Park, M.-S., Choi, Y.J., An, S.M., 2015. A study on the roughness length spatial distribution in relation to the Seoul building morphology. *Atmos.-Korea* 25, 339–351.
- Yu, C.-K., Smull, B.F., 2000. Airborne doppler observations of a landfalling cold front upstream of steep coastal orography. *Mon. Weather Rev.* 128, 1577–1603.
- Yue, C., Han, Z., Gu, W., Tang, Y., Ao, X., 2021. Research progress for dynamic effects of cities on precipitation: a review. *Atmosphere* 12, 1355.
- Zhang, T., Schultz, D.M., 2024. Cold-frontal rainbands over the United Kingdom: sensitivity of precipitation processes to microphysics schemes in WRF simulations. *Mon. Weather Rev.* 152, 2393–2418.
- Zhang, W., Villarini, G., Vecchi, G.A., Smith, J.A., 2018. Urbanization exacerbated the rainfall and flooding caused by hurricane Harvey in Houston. *Nature* 563, 384–388.
- Zhong, S., Yang, X.-Q., 2015a. Ensemble simulations of the urban effect on a summer rainfall event in the Great Beijing Metropolitan Area. *Atmos. Res.* 153, 318–334.
- Zhong, S., Yang, X.-Q., 2015b. Mechanism of urbanization impact on a summer cold-frontal rainfall process in the greater Beijing metropolitan area. *J. Appl. Meteorol. Climatol.* 54, 1234–1247.
- Zou, X., Cordeira, J.M., Bartlett, S.M., Kawzenuk, B., Roj, S., Castellano, C., Hecht, C., Ralph, F.M., 2023. Mesoscale and synoptic scale analysis of narrow cold frontal rainband during a landfalling atmospheric river in California during January 2021. *J. Geophys. Res. Atmos.* 128, e2023JD039426.